Perturbed Mitochondria-ER Contacts in Live Neurons Modelling Alzheimer's Disease Amyloid Pathology

Pamela V. Martino Adami [1,6], Zuzana Nichtová [2], David B. Weaver [2], Adam Bartok [2] Thomas Wisniewski [3], Drew R. Jones [4], Sonia Do Carmo [5], Eduardo M. Castaño [1], A. Claudio Cuello [5], György Hajnóczky[2], Laura Morelli [1]*.

[1]Laboratory of Brain Aging and Neurodegeneration, Fundación Instituto Leloir, IIBBA-CONICET, Av. Patricias Argentinas 435, C1405BWE, Ciudad Autónoma de Buenos Aires, Argentina.

[2]MitoCare Center for Mitochondrial Imaging Research and Diagnostics, Department of Pathology, Anatomy and Cell Biology, Thomas Jefferson University, Philadelphia, PA 19107, USA.

[3] Departments of Neurology, Pathology and Psychiatry, Center for Cognitive Neurology, NYU School of Medicine, New York, NY, USA.

[4] Metabolomics Core Resource Laboratory at NYU Langone Health

[5] Department of Pharmacology and Therapeutics, McGill University, McIntyre Medical Building 3655 Prom. Sir-William-Osler, Montreal, QC, H3G 1Y6, Canada.

[6]Division of Neurogenetics and Molecular Psychiatry, Department of Psychiatry and Psychotherapy, University of Cologne, 50937 Cologne, Germany.

*Corresponding author and Lead contact: Tel: +54-11-5238-7500, E-mail: lmorelli@leloir.org.ar

JCS Advance Online Article. Posted on 12 September 2019

SUMMARY STATEMENT

Mitochondria-ER contacts (MERC) upregulation was suggested as an underlying mechanism in Alzheimer`s disease (AD). Dynamic analysis of live neurons modelling AD-like amyloid pathology showed loosened mitochondria-ER apposition providing a novel perturbation of MERC axis in AD.

ABSTRACT

Reports using fixed fibroblasts from familial and sporadic Alzheimer's disease (AD) patients indicated upregulated mitochondria-endoplasmic reticulum contacts (MERC) as a hallmark of AD. Despite its potential significance, the relevance of these results is limited because they were not extended to live neurons. Here we performed a dynamic *in vivo* analysis of MERC in hippocampal neurons from McGill-R-Thy1-APP transgenic (Tg) rats, a model of AD-like amyloid pathology. Live FRET imaging in Tg revealed perturbed "lipid-MERC" (gap width <10 nm) while "Ca^{2+}-MERCs" (10-20 nm gap width) were unchanged. *In situ* TEM showed no significant differences in the percentage of lipid-MERC/Total MERC or lipid-MERCs/mitochondria number; however, the average length of lipid-MERC was significantly decreased in Tg as compared to controls. In accordance with FRET results, untargeted lipidomics showed significant decrements in the levels of 12 lipids and bioenergetic analysis revealed respiratory dysfunction of Tg mitochondria. Thus, our results reveal in AD-related neurons changes in MERC structure coupled with impaired mitochondrial functions.

KEYWORDS: Alzheimer; Transgenic Rats; Amyloid β/βCTF; Primary Neuronal Cultures; MERC; Mitochondrial Lipids; FRET

INTRODUCTION

Despite a plethora of studies that date back more than two decades, the early mechanisms that associate amyloid β (Aβ) accumulation with neuronal dysfunction in Alzheimer's disease (AD) have not been elucidated. However, bioenergetic failure has been suggested as an early event responsible for neuronal death in AD (Leuner et al., 2007; Mancuso et al., 2007; Mosconi et al., 2009; Kapogiannis and Mattson, 2011). It was shown that amyloid β precursor protein (APP) and Aβ co-localize with mitochondria (Mt) (Devi and Ohno, 2012; Hansson Petersen et al., 2008), that Aβ inhibits respiratory chain function (reviewed in (Swerdlow, 2012)) and that mitochondrial function also changes APP processing increasing or decreasing the production of amyloidogenic derivatives (Gabuzda et al., 1994; Gasparini et al., 1997; Leuner et al., 2012; Pereira et al., 1998). Apart from their essential role in bioenergetics, Mt are also involved in a great variety of other cellular processes, such as Ca^{2+} homeostasis and lipid biosynthesis. These functions require a dynamic spatial organization that allows signaling from and to other organelles. In particular, Mt are associated with the endoplasmic reticulum (ER) through contacts, Mt-ER contacts (MERC), that are formed between the outer mitochondrial membrane (OMM) and specialized regions of the ER, in which membrane and luminal components can intermix and exchange (Shore and Tata, 1977; Vance, 1990). These membranes can run in juxtaposition for hundreds of nanometers with a gap width between them of 5-30 nm when Mt are associated with smooth ER. The number, the interface length and the gap width are parameters regulated by the cell and may vary depending on the metabolic needs and the presence of stress agents (Bravo et al., 2011; Csordas et al., 2006; Sood et al., 2014).

Although many studies have investigated MERC in AD, none has analyzed in detail their number, interface length and structure in primary neurons in vivo. Moreover, neither much attention has been paid to the gap width between Mt and ER, which is an important structural parameter regulating the function of MERC in the transfer of ions and molecules between organelles (reviewed in Csordas et al., 2018; Giacomello and Pellegrini, 2016). It has already been shown that Mt can capture and accumulate Ca^{2+} to regulate the activity of enzymes that are central in energetic metabolism (Rizzuto et al., 2012; Hajnoczky et al., 1995; Jouaville et al., 1999; McCormack et al., 1990). The uptake of Ca^{2+} by the mitochondrial Ca^{2+} uniporter (MCU) (Baughman et al., 2011; De Stefani et al., 2011), although possible without the physical coupling

of the ER to Mt, is favored when the ER membrane is facing the OMM with a gap width of about 15 nm (Csordas et al., 2006; Csordas et al., 2010). For efficient Ca^{2+} transfer, the organelles would have to be separated by a distance of 10-25 nm (Ca^{2+}-MERC). In contrast, when lipids are being synthesized and exchanged in MERC (lipid-MERC), the organelles need their membranes to be in close proximity. Assuming that the density of the enzymes that synthesize lipids in these structures is homogeneous, any increase or decrease in MERC area should be accompanied by a similar change in the amount of lipids synthesized. Two models have been proposed to explain the transport of lipids between the two membranes: that lipids are transported by hydrophobic protein complexes, which would be interrupted in case the Mt-ER gap width is increased, or that lipids are coated by transporter proteins that diffuse from one membrane to the other, then an increase in the gap width would impact on the rate of delivery. In any case, the gap width required for lipid transfer is expected to be as narrow as ≤ 10 nm, given the proposed molecular mechanism implicated in the transfer of largely hydrophobic molecules between the organelles (Schauder et al., 2014).

In the last few years, some studies in cell lines, fibroblasts from AD patients (Area-Gomez et al., 2012; Del Prete et al., 2017) and zebrafish neuronal progenitors (Newman et al., 2017) have reported alterations in MERC, with contradictory results. However, none of them analyzed the gap width between the organelles in live neurons and with methods to evaluate proximity with the appropriate resolution. Moreover, the biochemical impact of altered MERC in primary neurons expressing endogenous Aβ has not been reported so far. The aim of this report was to perform a dynamic and ultrastructural analysis on hippocampal neurons of wild-type (WT) and McGill-R-Thy1-APP transgenic (Tg) rats by multicolor live imaging, using FRET generating drug-inducible interorganellar linkers (lateral resolution 8-10 nm), and by *in situ* transmission electron microscopy (TEM), respectively.

RESULTS

Neuronal expression of human Aβ peptides leads to time-dependent morphological alterations in mitochondria and endoplasmic reticulum.

McGill-R-Thy1-APP Tg neurons express the entire coding region of the human APP751 cDNA, including the familial AD Swedish double mutation (K670N, M671L) and the Indiana mutation (V717F) (Leon et al., 2010). We first determined, in the conditioned medium of days *in vitro* (DIV) 7 and DIV14 cultures (Supplementary Information Figure S1), the time-course accumulation of the three human Aβ isoforms and found that Aβ38, Aβ40 and Aβ42 were detectable (Figure 1 A), being the mean value of the extracellular levels of Aβ40 and of Aβ42 substantially lower, both at DIV7 (2.13 ± 0.5 pM and 0.63 ± 0.2 pM, respectively) and DIV14 (16.77 ± 4.92 pM and 4.47 ± 1.2 pM, respectively), than those previously reported in Swedish-type APP-HEK 293 transfected cells (~400 pM for Aβ40 and ~10 pM for Aβ42) (Ohshima et al., 2018), reinforcing the utility of this model to decipher cellular mechanisms involved in early stages of Aβ pathology. In agreement with what was described in cell culture experiments (Ohshima et al., 2018), Aβ monomers were not detected in cell lysates of Tg neurons by ELISA, suggesting an efficient clearance mechanism that precludes intraneuronal Aβ accumulation. To evaluate the impact of endogenous Aβ accumulation on neuronal ultrastructure, we performed TEM analysis. To avoid disturbances in the subcellular organization, TEM was carried out on neurons attached to coverslips. At DIV7, the morphology of Tg neurons was similar to that of WT neurons; while at DIV14, when the highest Aβ concentration in the conditioned medium was detected, Tg exhibited Mt with fragmented cristae and ER swelling (Figure 1B). It is of note that at DIV7 the number of Mt/soma (Figure 1C) and the ER lumen area (Figure 1D) were not significantly different between genotypes, while at DIV14, increments in the ER lumen area were detected as compared to DIV7 neurons regardless the presence of the human transgene.

To assess if levels of soluble Aβ isoforms detected in DIV7 Tg neurons could be associated with changes in the composition of endogenous free fatty acid (FFAs), known to modulate organelle membrane fluidity, oxidative stress and inflammation (Wang DC, 2012), we performed a targeted quantitative method for profiling FFAs in DIV7 WT and Tg neurons. To reach this aim we applied LC-MS to quantify and identify all the detectable FFAs present in neuronal homogenates. Six

FFAs were detected across the neuron samples, being palmitic acid, oleic acid and stearic acid by far the most abundant ones and roughly equal in concentration. A multiple t-test comparison was carried out between WT and Tg samples, but no significant ($p<0.05$) differences were observed for any of the FFAs (Supplementary Information Table S1).

Live neurons from Tg rats exhibit decreased coupling in lipid-MERC

To perform an *in vivo* analysis of neuronal MERC at early stages of Aβ pathology, without morphological alterations of Mt or ER and in the absence of disturbed lipid metabolism, we studied the pre-existing physiological MERC in live hippocampal neurons from WT and Tg rats at DIV7. To achieve this goal, we employed inducible interorganellar linkers tagged with CFP and YFP, respectively, which allow measurement of Mt-ER coupling in living cells with a resolution of 8-10 nm. We transfected neurons with rapamycin-inducible synthetic interorganellar, and upon expression of these constructs and rapamycin addition, a “bridge formation” was initially induced at the areas where the ER and the OMM were naturally close. CFP and YFP formed a FRET pair and the FRET signal confined to Mt-ER interface was visualized by multicolor epifluorescence microscopy. Rapamycin was applied only for a short time (<8 min) to minimize the broad effects initiated via mTOR, its endogenous receptor (Kim and Guan, 2015). Addition of rapamycin led to an immediate increase in the FRET signal and to a decrease in CFP fluorescence in both WT and Tg neuronal somata. In WT neurons, FRET/CFP ratio rapidly rose in a linear way until reaching a plateau at 200 sec (short linkers) (Figure 2A) or 150 sec (long linkers) (Figure 2B). In Tg neurons, FRET/CFP ratio with long linkers superimposed with that of WT (Figure 2B); while with short linkers, the curve was linear during all its trajectory without reaching a plateau (Figure 2A), indicating decreased Mt-ER coupling when the gap width is <10 nm.

Fixed neurons from Tg rats display similar percentage of lipid-MERCs but decreased length of apposition

To further test the Mt-ER interface, TEM images were quantified using an in-house-developed macro for Fiji (Weaver et al., 2017). The fixation was performed on cells attached to coverslips like the ones used for the live FRET imaging to conserve the characteristic morphology of the neurons. The analysis revealed that the percentage of lipid-MERC/total MERC (Figure 2C) and

the percentage of lipid-MERC/Mt number (Figure 2D) were similar between genotypes. However, we found that the length of ER-mitochondrial apposition (Sood et al., 2014) with a gap width <10 nm (lipid-MERC) was significantly reduced in Tg as compared to WT neurons (Figure 3B). Since the smaller length of apposition in Tg neurons could be the consequence of a decreased Mt size, we quantified the perimeter of Mt from WT and Tg neurons and found no significant differences between groups (Figure 3C). Moreover, the decrement in the interface length of apposition in lipid-MERC of Tg neurons persisted after normalizing it by the Mt perimeter (Figure 3D), suggesting that reduced length of apposition in lipid-MERC of Tg is not a consequence of altered mitochondrial morphology. Representative TEM micrographs depicting the interface length in WT and Tg are shown in Figure 3E. Thus, both the FRET and ultrastructure measurements support that the tight lipid-MERC is reduced in Tg neurons.

Decreased interface length in lipid-MERC is associated with alterations in mitochondrial lipid profile and bioenergetics functionality

In order to associate the decreased lipid-MERC with a biochemical read out, we isolated Mt from WT and Tg primary neurons (Supplementary Information Figure S2) and analyzed the lipid profile by lipidomics using high resolution LC-MS/MS. Lipid peaks were identified in each sample using LipidBlast (Kind et al., 2013), and the resulting hits were quantified using in-house scripts. The lipid profile of the mitochondrial extracts showed a significant deviation in the Tg group (Figure 4A). From the total number of lipids detected (n=106, Supplementary information Table S2), twelve different lipids were significantly different in Mt of Tg as compared to WT, exhibiting p-values ≤0.015 (Figure 4B). Among them, we found a 60%-decrement in major mitochondrial phospholipids cardiolipin (CL) and phosphatidylethanolamine (PE) in Mt preparations from Tg neurons as compared to WT, suggesting that alterations on lipid-MERC may have a direct impact on the biological relationship “membrane composition-structure-function” in Mt that may induce bioenergetic dysfunction.

In this regard, we assessed mitochondrial bioenergetics in intact neurons by extracellular flux analysis and found an altered bioenergetics profile (Figure 4C) and a significantly reduced spare respiratory capacity (Figure 4D) in Tg as compared to WT, suggesting a possible impairment in meeting a sudden increase in energy demand with increased ATP synthesis.

DISCUSSION

According to the Aβ levels detected in Tg neuronal cultures, we could speculate that our system represents a mild cellular model of AD-like amyloid pathology. The fact that we were unable to detect intracellular Aβ accumulation suggests that in embryonic primary neurons the degradation of aggregation-prone proteins, which are retained in the ER, is efficiently mediated by proteasome (Kostova and Wolf, 2003) and by insulin-degrading enzyme (Schmitz et al., 2004) activities. However, it is of note that we found morphological alterations of Mt and ER in DIV14 Tg neurons, similar to those reported in AD brains (Baloyannis, 2011), suggesting that extracellular Aβ peptides somehow impact on neuronal functionality. Mt swelling has been associated with the pathogenesis of AD; however, Mt alterations in neurons from AD brains were not related to the accumulation of amyloid deposits (Baloyannis, 2011). Even if we did not determine any parameter of the unfolded protein response (UPR) response in WT and Tg neurons at DIV7 and DIV14, we could speculate that Tg neurons at DIV14 show signs of activated UPR. The induction of artificial ER stress by overexpressing a membrane protein (as APP) must be considered as a possibility in our experimental setting, as previously reported (Hashimoto and Saido, 2018). However, the fact that the sub-cellular structure of Mt and ER is conserved in DIV7 Tg neurons, and that no significant differences were observed between genotypes for any of the six FFAs detected, suggests that the genetic (human APP expression) and environmental (extracellular Aβ accumulation) insults in Tg neurons at DIV7 are not enough to disturb the function of the ER and induce ER enlargement. In this regard, it was previously reported that exogenous palmitic acid decreases the expression of neurotrophic cytokines by inducing ER stress in SH-SY5Y human neuroblastoma cells, N2a mouse neuroblastoma cells, and cortices and hippocampi from wild-type C57BL/6J mice (Gurdeep Marwarha, 2016). Additional experiments are required in our cellular model to assess whether the significant ER enlargement detected in Tg neurons at DIV414 is mediated by increments of endogenous FFAs.

To our knowledge, this is the first report of MERC in live neurons using methods to evaluate proximity between these organelles with a lateral resolution of 8-10 nm. In a similar way, other studies have employed the same synthetic linkers to evaluate the physical extension and integrity of MERC in different cell lines, considering FRET signal as proportional to the extension of the Mt-ER apposition. Decreased Mt-ER coupling was also reported in caveolin-1 knock-out (Sala-

Vila et al., 2016) or mitofusin-2-ablated MEFs (Naon et al., 2016), reinforcing the validity of this genetic tool to assess altered Mt-ER interaction in live cells, although the effects of expression of synthetic linkers *per se* may need to be taken into account in any quantification (Shi et al., 2018). During the last five years, the concept that has dominated the field of MERC analysis in AD pathology was based on TEM, a "static" approach, suggesting an upregulated function of MERC that could induce mitochondrial bioenergetic dysfunction. However, this experimental evidence was never assessed in live primary neurons expressing endogenous Aβ peptides. MERC was evaluated in different AD-related models, such as *PSEN1* and/or *PSEN2-knock-out* MEFs and fibroblasts from familial and sporadic AD patients (Area-Gomez et al., 2012), neuroblastoma cell line SH-SY5Y overexpressing APP with the Swedish familial mutation (Del Prete et al., 2017), and mouse hippocampal primary neurons acutely exposed to synthetic Aβ peptides in the culture medium (Hedskog et al., 2013). In contrast to these studies, our "dynamic" and "static" results indicate that, at early stages of Aβ/APP fragments overproduction (without intraneuronal Aβ accumulation and conserved Mt and ER ultrastructure), there are no changes in Ca^{2+}-MERC, while a loosening of lipid-MERC apposition is evident. In agreement with our observation, in brain biopsies from patients with idiopathic normal pressure hydrocephalus, a neuropathology often associated with AD, it was described that the presence of both amyloid plaques and neurofibrillary tangles (AD pathological hallmarks) correlates with a decreased contact length between ER and Mt, analyzed by TEM (Leal et al, 2018). Even though they do not take into account the gap width between the organelles or study any biochemical impact of this alteration, their results support our observation in AD-like neurons of a decreased interface length in lipid-MERCs with a gap width <10 nm . In addition, lower numbers of MERC were reported in senescent cells (Janikiewicz et al., 2018), supporting the assumption that our cellular model may represent not only early stages of neuronal dysfunction associated to AD-amyloid pathology, but also aging.

The reasons for differences between our results of MERC analysis and the previous reports in AD-related *in vitro* models are not fully clear, but may be related to the cell type and methods used to quantify MERC. MERC were evaluated previously in fixed fibroblasts with confocal microscopy (lateral resolution is 250 nm) (Lidke and Lidke, 2012), or with proximity ligation assay (lateral resolution of >30 nm). These determinations were not performed in live cells and the techniques employed preclude an accurate quantification of the <10–30 nm distances that define

MERC. Even though Area-Gomez *et al.* (Area-Gomez et al., 2012) analyzed the interface length in fibroblasts from human subjects by TEM (a gold-standard methodology to evaluate inter-organelle distance), they did not assess the gap width between the ER and Mt. Finally, the results obtained using cells lines, even though they are informative, present limitations to infer what happens in live neurons. In this regard, Newman and colleagues recently analyzed by TEM the interface length, as previously reported in fibroblast from human subjects (Area-Gomez et al., 2012), in neuronal progenitors from zebrafish embryos injected with morpholines against *PSEN1* and/or *PSEN2*, and found no significant differences in *PSEN1/2 knock-down* cells as compared to controls (Newman et al., 2017), reinforcing the concept that MERC function and/or activity is cell-dependent, and although neurons share many features found in other cell types, they possess some special characteristics that cannot be reproduced in un-differentiated cells. Although Hedskog *et al.* (Hedskog et al., 2013) employed primary mouse hippocampal neurons, the increase in MERC number detected by confocal microscopy after acute synthetic Aβ exposure may represent an artefactual effect, since Aβ affects intracellular trafficking of Mt inducing accumulation of Mt in perinuclear regions, which are regions rich in ER (De Vos et al., 2008).

It has been already proposed that disturbances of MERC with a gap width <10 nm may impair lipid exchange between the ER and Mt (Giacomello and Pellegrini, 2016). In this report, we experimentally addressed this issue in primary neuronal cultures. It is known that Mt depend on the import of certain proteins and lipids for mitochondrial membrane formation and for maintaining cell bioenergetics. Although phosphatidylglycerol (PG), CL and PE are synthesized in Mt by specific enzymes, PC, phosphatidylinositol (PI), PS and sterols need to be imported from other organelles. The origin of most lipids imported into the Mt is the ER, which requires MERC properly assembled and functionally operational (Flis and Daum, 2013). Functionally, CL and PE interact with many mitochondrial proteins (Osman et al., 2011) and stabilize their conformation (Joshi et al., 2012), playing a crucial role in maintaining mitochondrial morphology. CL, the signature lipid of Mt, regulates mitochondrial bioenergetics due to its fundamental role in functional membrane assembly of redox complexes. It is of note that in this report we found that both CL levels and bioenergetics were altered in Tg neurons, reinforcing the a direct link between mitochondrial lipid composition and Mt functionality. Notably, Mt are the major supplier of PE to other organelles (Voelker, 1984), suggesting that reduction in the Mt content of PE as we showed in Tg samples,

may impact on neuronal functionality. We also detected a significant lower content of PC and PI in Tg as compared to WT, but in contrast to CL and PE, the specific functions of PC and PI are not well defined; however, their role in the maintenance of mitochondrial functionality seems to be indispensable (van Meer and Hoetzl, 2010). PC is the most abundant phospholipid in eukaryotic cells (van Meer et al., 2008), but given that Mt lack PC-synthesizing enzymes, it is imported from the ER. In a similar way, PI is produced in the ER and imported into Mt. On the whole, our results suggest that the decreased content of mitochondrial lipids might be a consequence of perturbed MERC apposition length.

In our model, different cellular events might be responsible for the reduced apposition between organelles. As it was previously proposed in cells overexpressing Tar DNA-binding proteins-43 (TDP-43), a major pathology in Amyotrophic Lateral Sclerosis with Associated Frontotemporal Dementia (ALS/FTD), loosening of MERC may be a consequence of the activation of glycogen synthase kinase 3β (GSK-3β), which then disrupts the binding of vesicle-associated membrane protein-associated protein B (VAPB) (located in the ER) to protein tyrosine phosphatase interacting protein 51 (PTPIP51) (resident in the OMM) (Stoica, R. et al. 2014). Increasing evidence suggests that GSK3 dysregulation is implicated in AD (DaRocha-Souto B et al. 2012), and all these findings support the idea that GSK3β is aberrantly activated by the presence of Aβ, and contributes, at least in part, to the neuronal anatomical derangement associated with Aβ pathology itself. Another mechanism, which in our case seems to be more improbable, is the "steric hindrance" that could cause the accumulation of Aβ oligomers (AβOs) on the OMM. Although we could not detect the presence of soluble Aβ isoforms in cell homogenates of Tg DIV7 neurons by ELISA, we cannot rule out the presence of intracellular AβOs. Further experiments using specific ELISA kits to detect AβOs will clarify this issue. Finally, it was reported that in addition to Aβ peptides, the production of β-secretase C-terminal fragment (βCTF) was also markedly increased in cells over-expressing the Swedish mutant APP (8-fold increase as compared to wild-type APP) (Forman et al., 1997). βCTF accumulation impacts on brain microsomes and Mt functionality (Kim et al., 1998; Chang and Suh, 2005), cellular events that may cause disturbances which ultimately lead to inappropriate organelle coupling. In addition, an alternative cause of an incompetent interaction between organelles may be the lipid composition of the membranes. In this regard, it was reported that the control of cellular cholesterol and

sphingomyelin (SM) metabolism involves APP processing, and that Aβ42 directly activates neutral sphingomyelinases and downregulates SM levels, whereas Aβ40 reduces cholesterol de novo synthesis by inhibition of hydroxymethylglutaryl-CoA reductase (HMGR) activity (Grimm et al., 2005).

Collectively, our results advance the current knowledge about the organization of MERC in neurons at early stages of AD-amyloid like pathology which will help to interpret functional roles of MERC axis in the context of AD.

MATERIALS AND METHODS

Ethical statements. This study was carried out in strict accordance with ARRIVE (Animal Research: Reporting of In Vivo Experiments) and OLAW-NIH (Office Laboratory Animal Welfare) guidelines. The protocols were approved by the local Animal Care Committee of Fundación Instituto Leloir (FIL) Assurance # A5168-01.

Reagents. Hank's Buffer Saline Solution (HBSS), trypsin-EDTA, DMEM/F12, Neurobasal, B27 and Lipofectamine 3000 were purchased from Thermo Scientific. Oligomycin, carbonyl cyanide-4-(trifluoromethoxy)phenylhydrazone (FCCP), antimycin A, rotenone and XF Medium were purchased from Seahorse Bioscience (Agilent). Poly-L-lysine and rapamycin were purchased from Merck.

Hippocampal primary neuronal cultures. Homozygous transgenic McGill-R-Thy1-APP (Tg+/+) rats, harboring the human APP751 transgene with the Swedish and Indiana mutation under the control of the murine Thy1.2 promoter, were generated using HsdBrl:WH Wistar strain (Leon et al., 2010). Animals were provided to FIL by The Royal Institution for the Advancement of Learning/McGill University, Montreal, Canada, and an in-house colony was established at FIL (Galeano et al., 2014). Cultures were performed as previously described (Ref), with minor modifications. Briefly, 10-12 embryos E18-19 were extracted from the uterus of pregnant WT or Tg+/+ rats, and hippocampi were isolated in HBSS buffer. Tissue was incubated with 2 mL of 0.25% trypsin-EDTA for 20 min at 37 °C and then washed 3 times with DMEM/F12-10% FBS. Hippocampi were homogenized in DMEM/F12-10% FBS by up and down-pipetting and viability was assessed with Trypan blue dye. Cells were plated in previously poly-L-lysine-coated dishes

and after 2 hours, medium was replaced by neuronal medium (Neurobasal, 2mM L-glutamine, 2% B27, 100 U/mL penicillin, 100 µg/mL streptomycin). Three days after plating (DIV3), AraC (cytosine β-D-arabinofuranoside) was added to conditioned medium at a final concentration of 1 µM to inhibit glia proliferation, yielding neuronal cultures with 92% purity. Neurons were maintained at 37°C in a humidified incubator with 5% CO_2 until DIV7-9 or DIV14-16.

Immunofluorescence. Neurons were cultured on 12 mm-diameter coverslips and fixed with 4% PFA at DIV7. Cells were then incubated with primary antibodies anti-βIII tubulin (mouse, 1:1000, Promega) and anti-Tom20 (rabbit,1:500, Santa Cruz), or GFAP (rabbit, 1:1000, Dako) overnight at 4°C, followed by incubation with secondary antibodies labelled with Alexa 488 or 546. Neurons were counterstained with DAPI to label nuclei.

Neuronal expression of Aβ isoforms. To quantify soluble Aβ 38/40/42, MSD® V-PLEX PLUS Aβ Peptide Panel 1 ELISA kit was used following the manufacturer's instructions. Conditioned media and protein homogenates were loaded in duplicates onto MULTI-SPOT® microplates pre-coated with antibodies specific to the C-termini of Aβ38, Aβ40 and Aβ42, and were detected with SULFO-TAG™-labeled 6E10 antibody. Light emitted upon electrochemical stimulation was read using the MSD QuickPlex SQ120 instrument. Data were analyzed using MSD Workbench 4.0 software.

LC-MS of Free Fatty Acids – Samples were subjected to an LCMS analysis to detect and quantify levels of free fatty acids in sample extracts. A fatty acid extraction was carried out on each sample using 100% methanol as the homogenization solvent. Cell pellets ($2x10^6$ cells/sample) were lysed with 500 µL of methanol and ~100 µL of zircon beads (0.5 mm). The methanol extracts were centrifuged (21,000g x 3 min) and transferred to glass LCMS inserts for analysis. The LC column was a Waters TM BEH-C18 (2.1 x100 mm, 1.7 µm) coupled to a Dionex Ultimate 3000TM system and the column oven temperature was set to 25oC for the gradient elution. The flow rate was 0.1 mL/min and used the following buffers; A) water with 0.1% formic acid and B) acetonitrile with 0.1% formic acid. The gradient profile was as follows; 35-35%B (0-5 min), 35-75%B (5-10 min), 75-99%B (10-10.25 min), 99-99%B (10.25-16.5 min), 99-35%B (16.5-16.75 min), 35-35%B (16.75-20 min). Injection volume was set to 1 µL for all analyses (20 min total run time per injection).

MS analyses were carried out by coupling the LC system to a Thermo Q Exactive HFTM mass spectrometer operating in heated electrospray ionization mode (HESI). Data acquisition was 10 min with a negative mode full MS scan (profile mode) and one microscan, with an AGC target of 3 x106 and a maximum IT of 100 ms at 120,000 resolution, with a scan range from 160-400 m/z. Spray voltage was 3.5kV and capillary temperature was set to 320oC with a sheath gas rate of 35, aux gas of 10, and max spray current of 100 µA. The acquisition order of samples and standard curve points was randomized, with blank matrix controls before and after each standard curve point to assess carry over (none detected). The resulting free fatty acid peaks were quantified by measuring the relative intensities (peak heights) of the high resolution extracted ion chromatogram (XIC) for each fatty acid across the samples and external standard curve samples. All fatty acids were detected as the negative mode [M-H]- ion and retention times of the fatty acids were defined using a cocktail of authentic standards. For each XIC, the theoretical m/z of each fatty acid (± 5 ppm) was used to extract the peak height (24 sec retention time window, 12 sec retention time tolerance) as follows: Lauric acid (199.1704 m/z, 2.3 min), Myristic acid (227.2017 m/z, 3.1 min), Palmitoleic acid (253.2173 m/z, 3.4 min), Palmitic acid (255.2330 m/z, 4.1 min), Oleic acid (281.2486 m/z, 4.4 min), Stearic acid (283.2643 m/z, 5.1 min), Arachidic acid (311.2956 m/z, 6.0 min), Nervonic acid (365.3425 m/z, 6.9 min), Lignoceric acid (367.3582 m/z, 7.5 min). The resulting standard curve points (in duplicate) were fit to a linear regression (GraphPad Prism7), and this equation was used to interpolate the concentration of fatty acids in the sample extracts, as prepared.

Neuronal bioenergetics. Sixty thousand cells per well were plated in Seahorse XFp Cell Culture Miniplates (Agilent) and were maintained in culture until DIV7, when bioenergetics was assessed. The day of the assay, conditioned medium was aspirated and replaced by XF Base Medium (Agilent) supplemented with 25 mM D-glucose, 1 mM sodium pyruvate and 2 mM L-glutamine (pH 7.4). Cells were incubated with this medium for 1 h at 37 °C in a non-CO_2 incubator, and then the microplate was loaded into Seahorse XFp Analyzer (Agilent) following manufacturer's guidelines. Oxygen consumption rate (OCR) was determined at the beginning of the assay (baseline OCR) and after the sequential addition of 2 µM oligomycin, 1 µM FCCP and 0.5 µM rotenone+antimycin A. In general, four baseline rates and three response rates (after the addition of a compound) were measured and the average of these rates used for data analysis. Neurons were titrated with

0.125-2 µM FCCP and 1 µM FCCP rendered the maximum OCR, so this concentration was used for the experiments. Non-mitochondrial OCR was determined after the addition of 0.5 µM rotenone+antimycin A and subtracted from all other values before calculation of the respiratory parameters as previously described [34]. Respiratory parameters were obtained as follows: basal respiration, baseline OCR; respiration driving proton leak, OCR after the addition of 2 mM oligomycin; respiration driving ATP synthesis, basal respiration – respiration driving proton leak; maximum respiration, OCR after the addition of 1 mM FCCP; respiratory control ratio (RCR), maximum respiration/respiration driving proton leak; spare respiratory capacity, maximum respiration – basal respiration; coupling efficiency, respiration driving ATP synthesis/basal respiration.

Plasmids and transfections. Neurons were plated on 25 mm-diameter coverslips and transfected at DIV5 using Lipofectamine 3000 (Thermo Scientific) with AKAP1-FKBP-YFP and CFP-FRB-ER ("short" linkers) or AKAP1-18x-FKBP-YFP and CFP-ER-9x-FRB ("long" linkers) plasmids. Mouse AKAP1 N-terminal sequence (residues 34-63: MAIQLRSLFPLALPGLLALLGWWWFFSRKK) targets outer mitochondrial membrane (OMM), and mouse Sac1 C-terminal sequence (residues 260-326: FLALPIIMVVAFSMCIICLLMAGDTWTETLAYVLFWGVASIGTFFIILYNGKDFVDAPRLVQKEKID) , the ER. Rapamycin-inducible heterodimerization domains, FKBP and FRB [35], were fused to AKAP1 and Sac1 sequences, respectively, through repetitive sequences which act like "arms", with a longer repetitive sequence for the long linkers and a shorter one for the short linkers. FKBP and FRB domains were also fused to fluorescent proteins YFP and CFP, respectively, which can form a FRET pair.

Multicolor live cell imaging. Forty-eight hours after transfection (DIV7), neuronal medium was replaced by imaging medium, composed by 50% fresh neuronal culture medium (Neurobasal, 2mM L-glutamine, 2% B27, 100 U/mL penicillin, 100 µg/mL streptomycin) and 50% ECM medium (120 mM NaCl, 5 mM $NaHCO_3$, 10 mM Na-HEPES, 4.7 mM KCl, 1.2 mM KH_2PO_4, 1.2 mM $MgSO_4$, 2 mM $CaCl_2$, 10 mM glucosa, 0.25% BSA, pH 7.4). Wide-field fluorescence was recorded at 37 °C with a ProEM1024 EM-CCD camera (Princeton Instruments) coupled to an epi-fluorescence inverted Leica DMI 6000B microscope with a 40x/NA 1.35 oil immersion objective (Olympus). The following filters were used: YFP (excitation: 495/20, emission: 532/54), CFP (excitation: 415/30,

emission: 502/38) and FRET (excitation: 415/30, emission: 532/54). Each triplet was obtained every 3 sec (to avoid photobleaching) during 7 min 30 sec (150 images). One-hundred nM rapamycin was added after the first 60 sec to induce the increase in FRET signal. Fluorescence was expressed as the FRET/CFP ratio after background subtraction of each individual wavelength using Spectralyzer software (Thomas Jefferson University, Philadelphia, USA). An average of ten measurements before the addition of rapamycin was subtracted from all other values of each individual experiment to normalize to basal FRET fluorescence.

Transmission electron microscopy. Neurons were plated on 15 mm-diameter coverslips until DIV7 or DIV14 and were fixed in cold 2% glutaraldehyde overnight. The following day, they were post-fixed in 1% osmium tetroxide, contrasted with 1% uranyl acetate, dehydrated with increasing ethanol concentrations and embedded in Durcupan. Blocks were immersed in liquid nitrogen to release the coverslips and they were then sliced into ultrathin sections. Sections were analyzed with a transmission electron microscope (Hitachi 7000). Gap width, interface length and mitochondrial perimeter analysis was performed with a macro for Fiji (Thomas Jefferson University, Philadelphia, USA), and ER lumen area with ImageJ.

Neuronal mitochondria isolation. Hippocampal primary neuronal cultures were prepared as described above, and after 7 days *in vitro*, cells were detached and mitochondria were isolated by differential centrifugation following standard procedures (Cadenas et al., 1980). Briefly, neurons were homogenized with a manual Teflon glass homogenizer in ice-cold MSTE buffer (0.23 M mannitol, 0.07 M sucrose, 10 mM Tris-HCl, 1 mM EDTA, pH 7.4). Homogenates were centrifuged at 600 x*g* for 10 min to discard cell debris and nuclei, and then supernatants were centrifuged at 8000 x*g* to obtain crude mitochondrial pellets. Protein concentration was determined with Pierce BCA Protein Assay Kit (Thermo Scientific).

Western blot. Samples (10 µg/lane) were run in SDS-Tricine 12.5% gels and transferred to a PVDF membrane. The membrane was blocked with 5% skim milk in PBS-Tween 0.01% for 1 h at room temperature and then incubated overnight at 4 °C with rabbit anti-Tom20 (1:500, Santa Cruz). Peroxidase-conjugated secondary antibody and enhanced chemiluminescence detection system (ECL, Thermo Scientific) were used to detect immunoreactivity which was quantitated with a STORM 840 Phosphor Imager (GE Healthcare).

LC-MS/MS with the global lipidomics method. Ten µg of mitochondrial samples were subjected to an LCMS analysis to detect and identify phospholipid molecules and quantify the relative levels of identified lipids. A lipid extraction was carried out on each sample based on the method by Vorkas *et al.*, (Vorkas et al., 2015a; Vorkas et al., 2015b). The dried samples were resolubilized in 10 µL of a 4:3:1 mixture (isopropanol:acetonitrile:water) and analyzed by UPLC-MS/MS with a polarity switching method modified from Vorkas *et al*. (Vorkas et al., 2015a; Vorkas et al., 2015b). The LC column was a WatersTM CSH-C18 (2.1 x100 mm, 1.7 µm) coupled to a Dionex Ultimate 3000TM system and the column oven temperature was set to 55°C for the gradient elution. The flow rate of 0.3 mL/min was used with the following buffers: A) 60:40 acetonitrile:water, 10 mM ammonium formate, 0.1% formic acid and B) 90:10 isopropanol:acetonitrile, 10 mM ammonium formate, 0.1% formic acid. The gradient profile was as follows: 40-43%B (0-1.25 min), 43-50%B (1.25-2 min), 50-54%B (2-11 min), 54-70%B (11-12 min), 70-99%B (12-18 min), 70-99%B (18-32min), 99-40%B (23-24 min), hold 40%B (1 min). Injection volume was set to 1 µL for all analyses (25 min total run time per injection). MS analyses were carried out by coupling the LC system to a Thermo Q Exactive HFTM mass spectrometer operating in heated electrospray ionization mode (HESI). Method duration was 20 min with a polarity switching data-dependent Top 10 method for both positive and negative modes. Spray voltage for both positive and negative modes was 3.5kV and capillary temperature was set to 320°C with a sheath gas rate of 35, aux gas of 10, and max spray current of 100 µA. The full MS scan for both polarities utilized 120,000 resolution with an AGC target of $3x10^6$ and a maximum IT of 100 ms, and the scan range was from 350-2000 m/z. Tandem MS spectra for both positive and negative mode used a resolution of 15,000, AGC target of $1x10^5$, maximum IT of 50 ms, isolation window of 0.4 m/z, isolation offset of 0.1 m/z, fixed first mass of 50 m/z, and 3-way multiplexed normalized collision energies (nCE) of 10, 35, 80. The minimum AGC target was $5x10^4$ with an intensity threshold of $1x10^6$. All data were acquired in profile mode and normalized to protein levels.

Statistical analysis. Data was expressed as media ± SEM of at least three independent experiments. Mean differences were analyzed with unpaired or paired Student's t-test or with two-way ANOVA test. Assumptions of normality and homoscedasticity were assessed with D'Agostino-Pearson omnibus normality test and with the F-test of equality of variances,

respectively. In some cases the assumption of homoscedasticity was violated and data were analyzed by Welch's unequal variances t-test. Significance level was set at $p<0.05$. Two-tailed probabilities were always reported. Statistical analysis was performed using GraphPad Prism 6 software (GraphPad software, Inc, La Jolla, CA)

AUTHOR CONTRIBUTIONS: Conceptualization, PVMA, GH and LM; Methodology, PVMA, ZN, DBW, AB, TW, SDC, AAC and GH; Investigation, PVMA and LM; Resources: LM, TW and GH; Validation, ZN, DBW and AB; Writing – Original Draft, PVMA and LM; Writing – Review and Editing, PVMA, SDC, EMC, ACC, GH and LM; Funding Acquisition, TW, EMC, ACC, GH and LM; Supervision, GH and LM.

ACKNOWLEDGMENTS: This study was supported by funding from the Agencia Nacional de Promoción Científica y Tecnológica (PICT-2015-0285, PICT-2016-4647 and PIBT/09-2013 to LM), International Society for Neurochemistry (CAEN Award 2016 to PVMA), International Union of Biochemistry and Molecular Biology (Wood-Whelan Fellowship 2016 to PVMA), Canadian Institutes of Health Research (201603PJT-364544 to ACC) and NIH grants (DK36609 and GM53407 to GH; AG008051, AG056850 and NS073502 to TW). PVMA was supported by CONICET fellowship. LM and EMC are members of the Research Career of CONICET. SDC is the holder of the Charles E. Frosst/Merck Research Associate position. ACC is member of the Canadian Consortium of Neurodegeneration in Aging (CCNA) and holder of the McGill University Charles E. Frosst/Merck Chair in Pharmacology. We acknowledge the helpful assistance of the NYU Metabolomics Core Resource Laboratory at New York University Langone Medical Center (USA) for the untargeted lipidomics analysis. Authors want to thank María Cecilia Rotondaro and Pablo Galeano from Leloir Institute for assistance in immunocytochemistry, confocal microscopy and statistical analysis, respectively.

DECLARATION OF INTERESTS: The authors declare that they have no conflict of interest.

REFERENCES

- Area-Gomez, E., Del Carmen Lara Castillo, M., Tambini, M.D., Guardia-Laguarta, C., de Groof, A.J., Madra, M., Ikenouchi, J., Umeda, M., Bird, T.D., Sturley, S.L., *et al.* (2012). Upregulated function of mitochondria-associated ER membranes in Alzheimer disease. EMBO J *31*, 4106-4123.
- Baloyannis, S.J. (2011). Mitochondria are related to synaptic pathology in Alzheimer's disease. Int J Alzheimers Dis *2011*, 305395.
- Baughman, J.M., Perocchi, F., Girgis, H.S., Plovanich, M., Belcher-Timme, C.A., Sancak, Y., Bao, X.R., Strittmatter, L., Goldberger, O., Bogorad, R.L., *et al.* (2011). Integrative genomics identifies MCU as an essential component of the mitochondrial calcium uniporter. Nature *476*, 341-345.
- Bravo, R., Vicencio, J.M., Parra, V., Troncoso, R., Munoz, J.P., Bui, M., Quiroga, C., Rodriguez, A.E., Verdejo, H.E., Ferreira, J., *et al.* (2011). Increased ER-mitochondrial coupling promotes mitochondrial respiration and bioenergetics during early phases of ER stress. J Cell Sci *124*, 2143-2152.
- Cadenas, E., Boveris, A., and Chance, B. (1980). Low-level chemiluminescence of bovine heart submitochondrial particles. Biochem J *186*, 659-667.
- Csordas, G., Renken, C., Varnai, P., Walter, L., Weaver, D., Buttle, K.F., Balla, T., Mannella, C.A., and Hajnoczky, G. (2006). Structural and functional features and significance of the physical linkage between ER and mitochondria. J Cell Biol *174*, 915-921.
- Csordas, G., Varnai, P., Golenar, T., Roy, S., Purkins, G., Schneider, T.G., Balla, T., and Hajnoczky, G. (2010). Imaging interorganelle contacts and local calcium dynamics at the ER-mitochondrial interface. Mol Cell *39*, 121-132.
- Csordas, G., Weaver, D., and Hajnoczky, G. (2018). Endoplasmic Reticulum-Mitochondrial Contactology: Structure and Signaling Functions. Trends Cell Biol *28*, 523-540.
- Chang, K.A., and Suh, Y.H. (2005). Pathophysiological roles of amyloidogenic carboxy-terminal fragments of the beta-amyloid precursor protein in Alzheimer's disease. Journal of pharmacological sciences *97*, 461-471.

— DaRocha-Souto B, Coma M, Pérez-Nievas BG, Scotton TC, Siao M, Sánchez-Ferrer P, Hashimoto T, Fan Z, Hudry E, Barroeta I, Serenó L, Rodríguez M, Sánchez MB, Hyman BT, Gómez-Isla T. (2012) Activation of glycogen synthase kinase-3 beta mediates β-amyloid induced neuritic damage in Alzheimer's disease. Neurobiol Dis. *45*:425–437

— De Stefani, D., Raffaello, A., Teardo, E., Szabo, I., and Rizzuto, R. (2011). A forty-kilodalton protein of the inner membrane is the mitochondrial calcium uniporter. Nature *476*, 336-340.

— De Vos, K.J., Grierson, A.J., Ackerley, S., and Miller, C.C. (2008). Role of axonal transport in neurodegenerative diseases. Annu Rev Neurosci *31*, 151-173.

— Del Prete, D., Suski, J.M., Oules, B., Debayle, D., Gay, A.S., Lacas-Gervais, S., Bussiere, R., Bauer, C., Pinton, P., Paterlini-Brechot, P.*, et al.* (2017). Localization and Processing of the Amyloid-beta Protein Precursor in Mitochondria-Associated Membranes. J Alzheimers Dis *55*, 1549-1570.

— Devi, L., and Ohno, M. (2012). Mitochondrial dysfunction and accumulation of the beta-secretase-cleaved C-terminal fragment of APP in Alzheimer's disease transgenic mice. Neurobiol Dis *45*, 417-424.

— Flis, V.V., and Daum, G. (2013). Lipid transport between the endoplasmic reticulum and mitochondria. Cold Spring Harbor perspectives in biology *5*.

— Forman, M.S., Cook, D.G., Leight, S., Doms, R.W., and Lee, V.M. (1997). Differential effects of the swedish mutant amyloid precursor protein on beta-amyloid accumulation and secretion in neurons and nonneuronal cells. J Biol Chem *272*, 32247-32253.

— Gabuzda, D., Busciglio, J., Chen, L.B., Matsudaira, P., and Yankner, B.A. (1994). Inhibition of energy metabolism alters the processing of amyloid precursor protein and induces a potentially amyloidogenic derivative. J Biol Chem *269*, 13623-13628.

— Galeano, P., Martino Adami, P.V., Do Carmo, S., Blanco, E., Rotondaro, C., Capani, F., Castano, E.M., Cuello, A.C., and Morelli, L. (2014). Longitudinal analysis of the behavioral phenotype in a novel transgenic rat model of early stages of Alzheimer's disease. Frontiers in behavioral neuroscience *8*, 321.

— Gasparini, L., Racchi, M., Benussi, L., Curti, D., Binetti, G., Bianchetti, A., Trabucchi, M., and Govoni, S. (1997). Effect of energy shortage and oxidative stress on amyloid precursor protein metabolism in COS cells. Neurosci Lett *231*, 113-117.

— Giacomello, M., and Pellegrini, L. (2016). The coming of age of the mitochondria-ER contact: a matter of thickness. Cell Death Differ *23*, 1417-1427.

— Grimm, M.O., Grimm, H.S., Patzold, A.J., Zinser, E.G., Halonen, R., Duering, M., Tschape, J.A., De Strooper, B., Muller, U., Shen, J.*, et al.* (2005). Regulation of cholesterol and sphingomyelin metabolism by amyloid-beta and presenilin. Nat Cell Biol *7*, 1118-1123.

— Gurdeep Marwarha et al, (2016) Palmitate-induced Endoplasmic Reticulum stress and subsequent C/EBPα Homologous Protein activation attenuates leptin and Insulin-like Growth Factor 1 expression in the brain. Cell Signal, 28, 1789–1805.

— Hajnoczky, G., Robb-Gaspers, L.D., Seitz, M.B., and Thomas, A.P. (1995). Decoding of cytosolic calcium oscillations in the mitochondria. Cell *82*, 415-424.

— Hansson Petersen, C.A., Alikhani, N., Behbahani, H., Wiehager, B., Pavlov, P.F., Alafuzoff, I., Leinonen, V., Ito, A., Winblad, B., Glaser, E.*, et al.* (2008). The amyloid beta-peptide is imported into mitochondria via the TOM import machinery and localized to mitochondrial cristae. Proc Natl Acad Sci U S A *105*, 13145-13150.

— Hashimoto, S., and Saido, T.C. (2018). Critical review: involvement of endoplasmic reticulum stress in the aetiology of Alzheimer's disease. Open biology *8*.

— Hedskog, L., Pinho, C.M., Filadi, R., Ronnback, A., Hertwig, L., Wiehager, B., Larssen, P., Gellhaar, S., Sandebring, A., Westerlund, M.*, et al.* (2013). Modulation of the endoplasmic reticulum-mitochondria interface in Alzheimer's disease and related models. Proc Natl Acad Sci U S A *110*, 7916-7921.

— Janikiewicz, J., Szymański, J., Malinska,D., Patalas-Krawczyk, P.,Michalska,B.,Duszyński, J., Giorgi, C.,Bonora, M., Dobrzyn, A., and Wieckowski, M.R. (2018) Mitochondria-associated membranes in aging and senescence: structure, function, and dynamics. Cell Death & Disease *9*,2-12.

— Joshi, A.S., Thompson, M.N., Fei, N., Huttemann, M., and Greenberg, M.L. (2012). Cardiolipin and mitochondrial phosphatidylethanolamine have overlapping functions in mitochondrial fusion in Saccharomyces cerevisiae. J Biol Chem *287*, 17589-17597.

— Jouaville, L.S., Pinton, P., Bastianutto, C., Rutter, G.A., and Rizzuto, R. (1999). Regulation of mitochondrial ATP synthesis by calcium: evidence for a long-term metabolic priming. Proc Natl Acad Sci U S A *96*, 13807-13812.

— Kapogiannis, D., and Mattson, M.P. (2011). Disrupted energy metabolism and neuronal circuit dysfunction in cognitive impairment and Alzheimer's disease. Lancet Neurol *10*, 187-198.

— Kim, H.S., Park, C.H., and Suh, Y.H. (1998). C-terminal fragment of amyloid precursor protein inhibits calcium uptake into rat brain microsomes by Mg2+-Ca2+ ATPase. Neuroreport *9*, 3875-3879.

— Kim, Y.C., and Guan, K.L. (2015). mTOR: a pharmacologic target for autophagy regulation. The Journal of clinical investigation *125*, 25-32.

— Kind, T., Liu, K.H., Lee, D.Y., DeFelice, B., Meissen, J.K., and Fiehn, O. (2013). LipidBlast in silico tandem mass spectrometry database for lipid identification. Nature methods *10*, 755-758.

— Kostova, Z., and Wolf, D.H. (2003). For whom the bell tolls: protein quality control of the endoplasmic reticulum and the ubiquitin-proteasome connection. EMBO J *22*, 2309-2317.

— Leal, N.S, Dentoni, G., Schreiner, B,, Kämäräinen, O.P., Partanen, N,, Herukka, S.K., Koivisto, A.M., Hiltunen, M., Rauramaa, T., Leinonen, V., and Ankarcrona, M. (2018). Alterations in mitochondria-endoplasmic reticulum connectivity in human brain biopsies from idiopathic normal pressure hydrocephalus patients. Acta Neuropathol Commun *6*, 1-9

— Leon, W.C., Canneva, F., Partridge, V., Allard, S., Ferretti, M.T., DeWilde, A., Vercauteren, F., Atifeh, R., Ducatenzeiler, A., Klein, W.*, et al.* (2010). A novel transgenic rat model with a full Alzheimer's-like amyloid pathology displays pre-plaque intracellular amyloid-beta-associated cognitive impairment. J Alzheimers Dis *20*, 113-126.

— Leuner, K., Hauptmann, S., Abdel-Kader, R., Scherping, I., Keil, U., Strosznajder, J.B., Eckert, A., and Muller, W.E. (2007). Mitochondrial dysfunction: the first domino in brain aging and Alzheimer's disease? Antioxid Redox Signal *9*, 1659-1675.

— Leuner, K., Schutt, T., Kurz, C., Eckert, S.H., Schiller, C., Occhipinti, A., Mai, S., Jendrach, M., Eckert, G.P., Kruse, S.E., *et al.* (2012). Mitochondrion-derived reactive oxygen species lead to enhanced amyloid beta formation. Antioxid Redox Signal *16*, 1421-1433.

— Lidke, D.S., and Lidke, K.A. (2012). Advances in high-resolution imaging--techniques for three-dimensional imaging of cellular structures. J Cell Sci *125*, 2571-2580.

— Mancuso, M., Coppede, F., Murri, L., and Siciliano, G. (2007). Mitochondrial cascade hypothesis of Alzheimer's disease: myth or reality? Antioxid Redox Signal *9*, 1631-1646.

— McCormack, J.G., Halestrap, A.P., and Denton, R.M. (1990). Role of calcium ions in regulation of mammalian intramitochondrial metabolism. Physiol Rev *70*, 391-425.

— Mosconi, L., Mistur, R., Switalski, R., Tsui, W.H., Glodzik, L., Li, Y., Pirraglia, E., De Santi, S., Reisberg, B., Wisniewski, T., *et al.* (2009). FDG-PET changes in brain glucose metabolism from normal cognition to pathologically verified Alzheimer's disease. Eur J Nucl Med Mol Imaging *36*, 811-822.

— Naon, D., Zaninello, M., Giacomello, M., Varanita, T., Grespi, F., Lakshminaranayan, S., Serafini, A., Semenzato, M., Herkenne, S., Hernandez-Alvarez, M.I., *et al.* (2016). Critical reappraisal confirms that Mitofusin 2 is an endoplasmic reticulum-mitochondria tether. Proc Natl Acad Sci U S A *113*, 11249-11254.

— Newman, M., Halter, L., Lim, A., and Lardelli, M. (2017). Mitochondrion to endoplasmic reticulum apposition length in zebrafish embryo spinal progenitors is unchanged in response to perturbations associated with Alzheimer's disease. PLoS One *12*, e0179859.

— Ohshima, Y., Taguchi, K., Mizuta, I., Tanaka, M., Tomiyama, T., Kametani, F., Yabe-Nishimura, C., Mizuno, T., and Tokuda, T. (2018). Mutations in the beta-amyloid precursor protein in familial Alzheimer's disease increase Abeta oligomer production in cellular models. Heliyon *4*, e00511.

— Osman, C., Voelker, D.R., and Langer, T. (2011). Making heads or tails of phospholipids in mitochondria. J Cell Biol *192*, 7-16.

— Pereira, C., Santos, M.S., and Oliveira, C. (1998). Mitochondrial function impairment induced by amyloid beta-peptide on PC12 cells. Neuroreport *9*, 1749-1755.

— Rizzuto, R., De Stefani, D., Raffaello, A., and Mammucari, C. (2012). Mitochondria as sensors and regulators of calcium signalling. Nat Rev Mol Cell Biol *13*, 566-578.

— Sala-Vila, A., Navarro-Lerida, I., Sanchez-Alvarez, M., Bosch, M., Calvo, C., Lopez, J.A., Calvo, E., Ferguson, C., Giacomello, M., Serafini, A., *et al.* (2016). Interplay between hepatic mitochondria-associated membranes, lipid metabolism and caveolin-1 in mice. Scientific reports *6*, 27351.

— Schauder, C.M., Wu, X., Saheki, Y., Narayanaswamy, P., Torta, F., Wenk, M.R., De Camilli, P., and Reinisch, K.M. (2014). Structure of a lipid-bound extended synaptotagmin indicates a role in lipid transfer. Nature *510*, 552-555.

— Schmitz, A., Schneider, A., Kummer, M.P., and Herzog, V. (2004). Endoplasmic reticulum-localized amyloid beta-peptide is degraded in the cytosol by two distinct degradation pathways. Traffic *5*, 89-101.

— Shi, F., Kawano, F., Park, S.E., Komazaki, S., Hirabayashi, Y., Polleux, F., and Yazawa, M. (2018) Optogenetic Control of Endoplasmic Reticulum-Mitochondria Tethering. ACS Synthetic Biology *7*, 2-9.

— Shore, G.C., and Tata, J.R. (1977). Two fractions of rough endoplasmic reticulum from rat liver. I. Recovery of rapidly sedimenting endoplasmic reticulum in association with mitochondria. J Cell Biol *72*, 714-725.

— Sood, A., Jeyaraju, D.V., Prudent, J., Caron, A., Lemieux, P., McBride, H.M., Laplante, M., Toth, K., and Pellegrini, L. (2014). A Mitofusin-2-dependent inactivating cleavage of Opa1 links changes in mitochondria cristae and ER contacts in the postprandial liver. Proc Natl Acad Sci U S A *111*, 16017-16022.

— Stoica, R. De Vos, K.J, Paillusson, S. Mueller, S. Sancho, R.M., Lau, K.F., Vizcay-Barrena, G., Lin, W.L., Xu, Y-F., Lewis, J., Dickson, D.W., Petrucelli, L., Mitchell, J.C., Shaw, C.E., and Miller C.C.J. (2014) ER-mitochondria associations are regulated by the VAPB-PTPIP51 interaction and are disrupted by ALS/FTD-associated TDP-43. Nat. Commun. *5*, 3996

— Swerdlow, R.H. (2012). Mitochondria and cell bioenergetics: increasingly recognized components and a possible etiologic cause of Alzheimer's disease. Antioxid Redox Signal *16*, 1434-1455.

— van Meer, G., and Hoetzl, S. (2010). Sphingolipid topology and the dynamic organization and function of membrane proteins. FEBS Lett *584*, 1800-1805.

— van Meer, G., Voelker, D.R., and Feigenson, G.W. (2008). Membrane lipids: where they are and how they behave. Nat Rev Mol Cell Biol *9*, 112-124.

— Vance, J.E. (1990). Phospholipid synthesis in a membrane fraction associated with mitochondria. J Biol Chem *265*, 7248-7256.

— Vance, J.E. (2014). MAM (mitochondria-associated membranes) in mammalian cells: lipids and beyond. Biochim Biophys Acta *1841*, 595-609.

— Voelker, D.R. (1984). Phosphatidylserine functions as the major precursor of phosphatidylethanolamine in cultured BHK-21 cells. Proc Natl Acad Sci U S A *81*, 2669-2673.

— Vorkas, P.A., Isaac, G., Anwar, M.A., Davies, A.H., Want, E.J., Nicholson, J.K., and Holmes, E. (2015a). Untargeted UPLC-MS profiling pipeline to expand tissue metabolome coverage: application to cardiovascular disease. Anal Chem *87*, 4184-4193.

— Vorkas, P.A., Shalhoub, J., Isaac, G., Want, E.J., Nicholson, J.K., Holmes, E., and Davies, A.H. (2015b). Metabolic phenotyping of atherosclerotic plaques reveals latent associations between free cholesterol and ceramide metabolism in atherogenesis. J Proteome Res *14*, 1389-1399.

— Wang D.C., Sun C.H.,Liu L.H,, Sun X.H., Jin X.W,, Song W.L,, Liu X.Q,, Wan X.L. (2012) Serum fatty acid profiles using GC-MS and multivariate statistical analysis: potential biomarkers of Alzheimer's disease Neurobiology of Aging, 33, 1057-1066

— Weaver, D., Bartok, A., Csordas, G. and Hajnoczky, G. (2017). A Standardized Method to Quantify ER-Mitochondrial Interfaces in Electron Mircographs. Biophysical Journal *112*, Special Issue 3, 133A DOI:https://doi.org/10.1016/j.bpj.2016.11.735

Figures

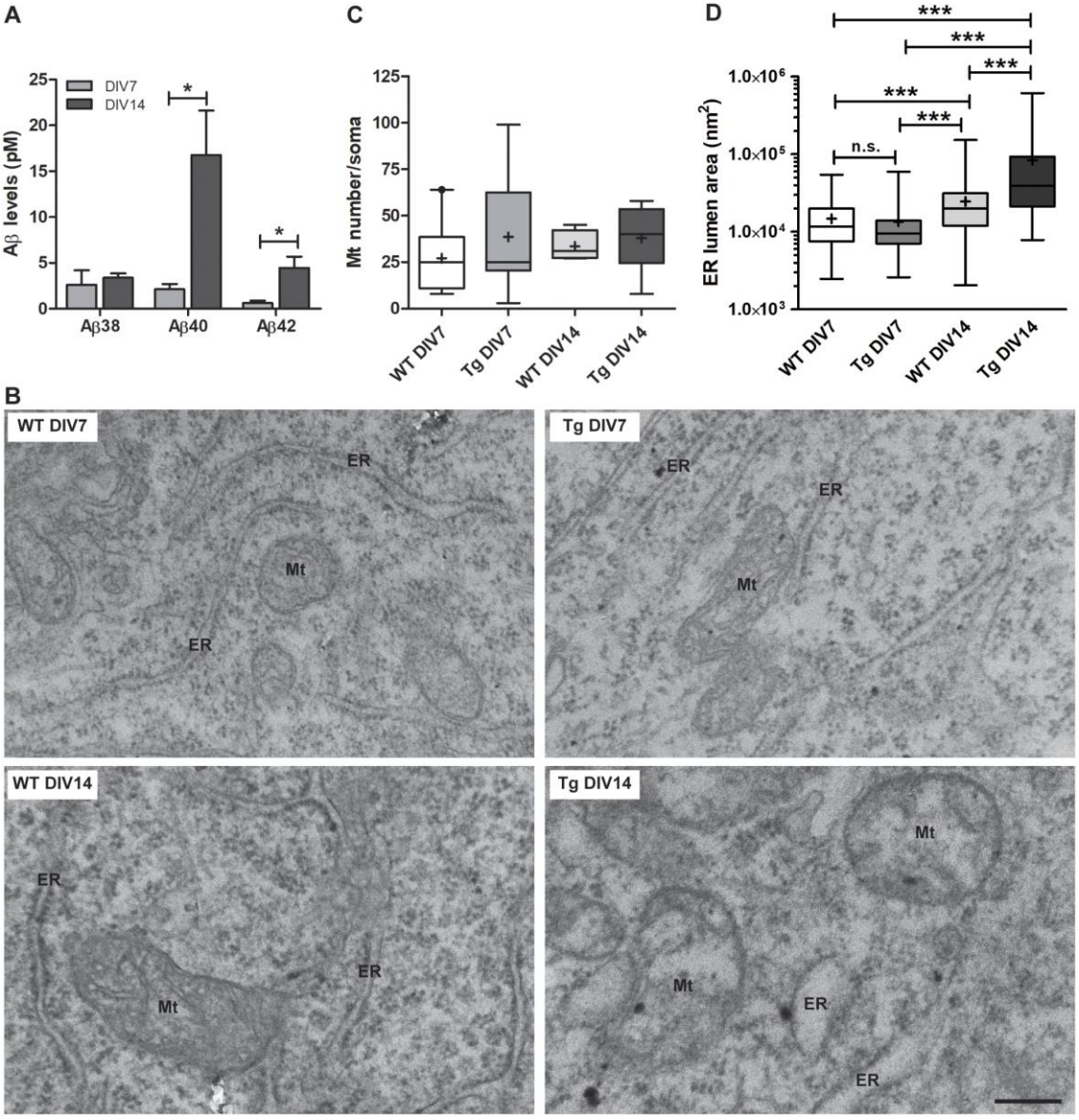

Figure 1

Hippocampal primary neurons from Tg rats produce human Aβ isoforms and show mitochondria and endoplasmic reticulum swelling after 14 days *in vitro*. A) Quantification of Aβ levels in neuronal conditioned medium. Bars indicate the concentration (in pM) of each Aβ isoform in the conditioned media of days *in vitro* (DIV) 7 or 14 transgenic neurons from three different independent cultures/genotype. Unpaired two-tailed Student's t test (Aβ38: p=0.610; Aβ40: p=0.040; Aβ42: p=0.035) was used for comparison between DIV. **B)** Representative

transmission electron microphotographs showing mitochondria and endoplasmic reticulum ultrastructure in coverslip-attached embryonic primary hippocampal neurons from WT rats with 7 days (upper left panel) or 14 days *in vitro* (lower left panel), and from Tg rats with 7 days (upper right panel) or 14 days *in vitro* (lower right panel). Scale bar, 250 nm. **C)** Mitochondria number quantification in neuronal somata. Three independent hippocampal primary neuronal cultures were performed for each genotype using 10-12 embryos/culture. Data were obtained after processing coverslip-attached primary cultures from WT and Tg rats DIV7 or DIV14 by TEM (WT DIV7: N=9 cells; Tg DIV7: N=9 cells; WT DIV14: N=4 cells; Tg DIV14: N=8 cells) (Two-way ANOVA: DIV: $F=0.1$, $p=0.749$; Genotype: $F=0.78$, $p=0.385$; DIV x Genotype: $F=0.15$, $p=0.704$). Mt, mitochondria; DIV, days *in vitro*; TEM, transmission electron microscopy. **D)** Endoplasmic reticulum lumen area quantification in the same neuronal somata as in **C)**. Kruskal-Wallis test ($p<0.0001$) followed by Dunn's post-hoc test. ***$p<0.001$. ER, endoplasmic reticulum; DIV, days *in vitro*.

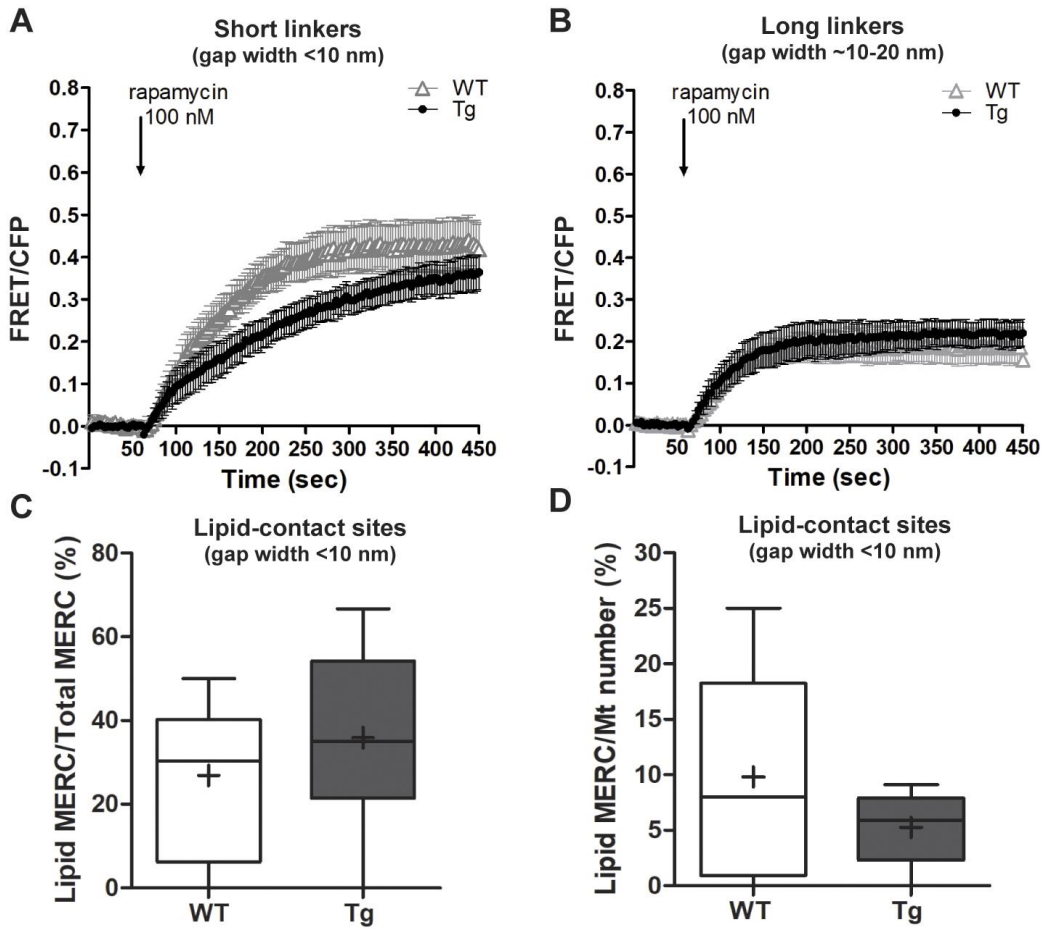

Figure 2

Lipid-MERC is decreased in live hippocampal primary neurons from Tg rats Upper panels, traces showing the FRET ratio (FRET/CFP) before and after induction of the linkage by rapamycin (addition is marked by an arrow) in WT and Tg neurons. **A)** FRET ratio with short linkers (gap width <10 nm) and **B)** FRET ratio with long linkers (gap width ~10-20 nm). Calculations were made for neuronal somata. Independent hippocampal primary neuronal cultures (n=3 for WT; n=4 for Tg) were performed using 10-12 embryos/culture. Data were obtained from 9-17 cells per group. Morphometric analysis of lipid-contact sites (<10 nm) in transmission electron microphotographs. Bars show percentage of lipid-MERC (<10 nm)/total MERCS (10 nm to 30 nm) **(C)** and percentage of lipid-MERC (<10 nm)/mitochondria number **(D).**

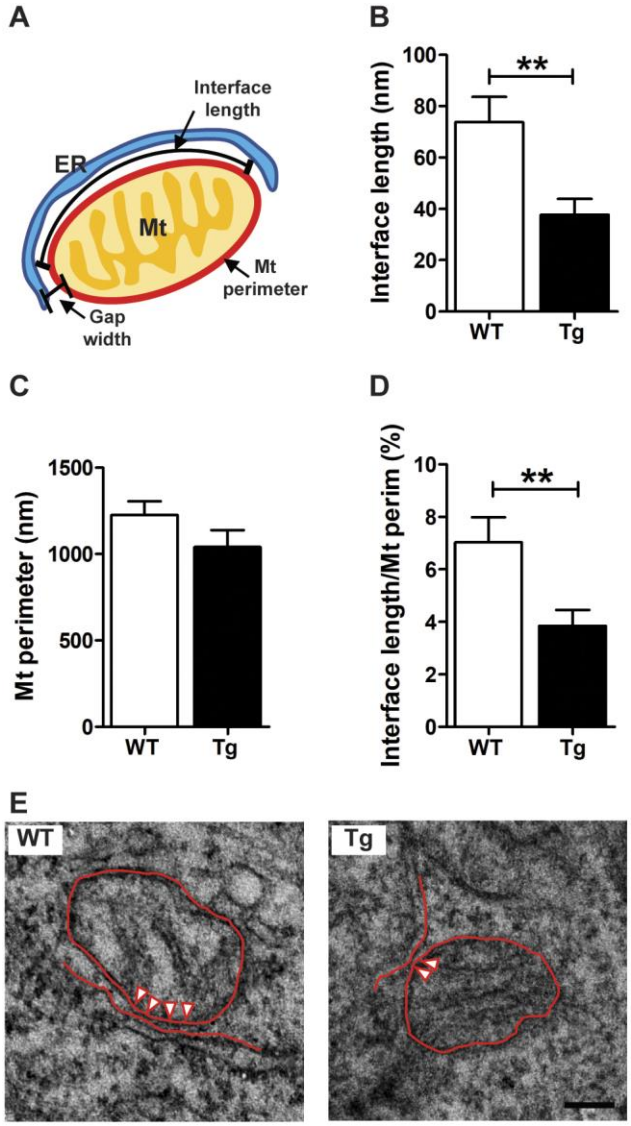

Figure 3

Tg neurons with 7 days *in vitro* display decreased interface length in lipid-MERC. Coverslip-attached neurons were subjected to transmission electron microscopy to analyze the MERC structural parameters depicted in **A). B)** Bars show the quantification of the interface length with a gap width <10 nm. Unpaired two-tailed Student's t test with Welch's correction (t=3.112, p=0.003). **C)** Mitochondrial perimeter of the same mitochondria involved in **B)**. Data were analyzed by unpaired two-tailed Student's t test (t=1.393, p=0.168). **D)** Ratio between interface length and mitochondrial perimeter from **B)** and **C)**, respectively. Unpaired two-tailed Student's t test with Welch's correction (t=2.804, p=0.007) was employed. **E)** Representative microphotographs showing MERC. The interface where the gap width is <10 nm is indicated by

arrowheads. All calculations were made for neuronal somata. Analysis was performed in WT (n=13) and Tg (n= 16) cells. The number of evaluated Mt was n=47 for WT and n=21 for Tg. Cells come from 3 different cultures/genotype using 10-12 embryos/culture. ER, endoplasmic reticulum; Mt, mitochondria; perim, perimeter. Scale bar, 100 nm.

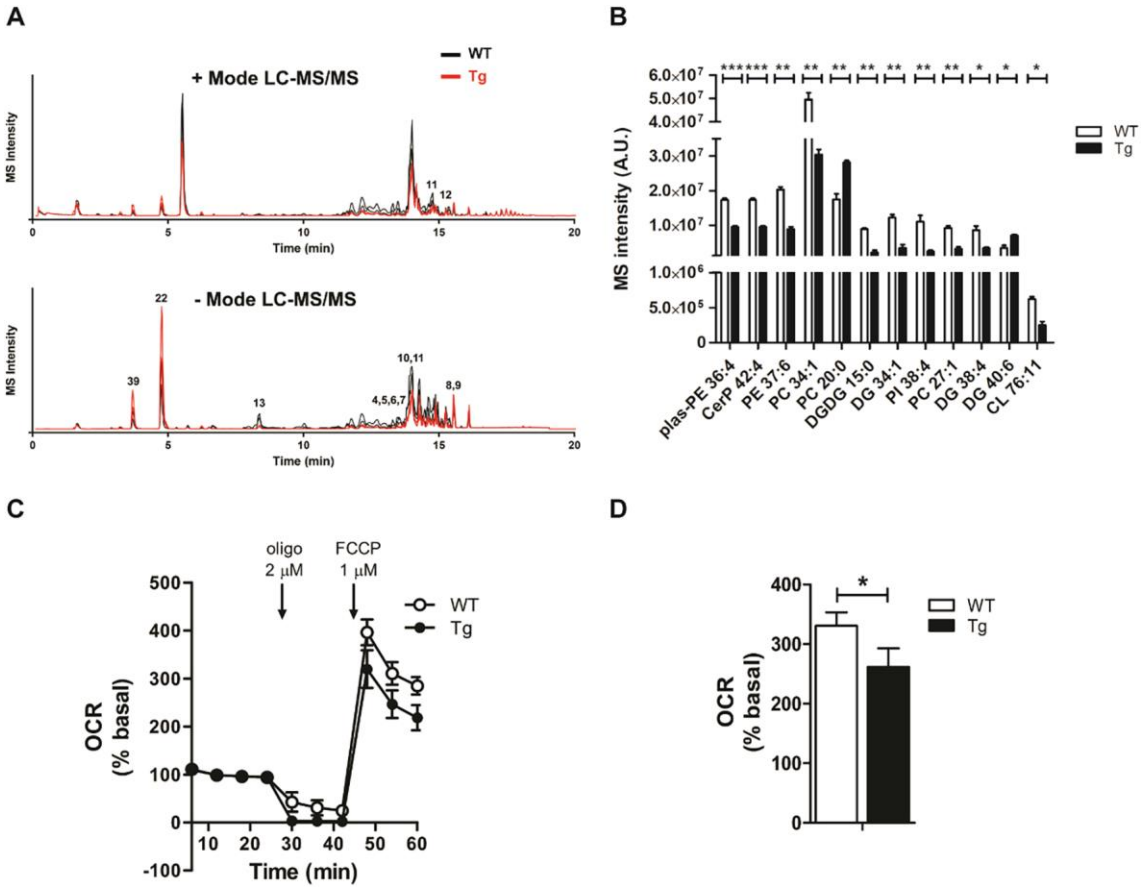

Figure 4

Alterations in mitochondrial lipid profile impact on mitochondrial bioenergetics functionality in Tg neurons with 7 days *in vitro*. A) Base-peak chromatogram of detected lipids by positive (upper panel) and negative (lower panel) mode untargeted LC-MS/MS, scan range = 350-2000 m/z. Lipid retention time is shown on the horizontal axis while peak intensity is shown on the vertical axis. Each profile represents an overlay of the samples tested (n=3 per genotype). Numbers indicate the lipid peaks (listed below) with significant differences between WT and Tg. **B)** Bars show the MS intensity in arbitrary units (A.U.) of the 12 lipids in Tg that exhibited significant differences with a p-value ≤0.015. ***p<0.001, **p<0.01, *p<0.05. Peak 4, Plasmenyl-PE 36:4; Peak 5, CerP 32:4; Peak 6, PE 37:6, Peak 7, PC 34:1; Peak 8, PC 20; 0; Peak 9, DGDG 15:0. Peak 10, PC 33:5; Peak 11, PC 31:4; Peak 12, DG 31:4; Peak 13, PI 38:4; Plasm-PE, plasmenyl-PE; PC, phosphatidylcholine; DG, diacylglycerol; PI, phosphatidylinositol; PE, phosphatidylethanolamine; CerP, ceramide-1-phosphate; DGDG, digalactosyldiacylglycerol; CL, cardiolipin. **C)** Bioenergetic profile of days *in vitro* (DIV) 7 WT and Tg neurons assessed with an

extracellular flux analyser. Oxygen consumption rate (OCR) was normalized to the mean value of the four baseline measurements (100%), before the addition of inhibitors or the uncoupler, and after subtraction of non-mitochondrial respiration. **D)** Bars show the spare respiratory capacity calculated as the difference between maximal and baseline OCR from the same cells as in **A)**. Oligo, oligomycin; FCCP, carbonyl cyanide-4-phenylhydrazone. Three independent cultures/genotype were performed. Paired two-tailed Student's t test (t=6.479, *p=0.023) was used for comparisons between genotypes.

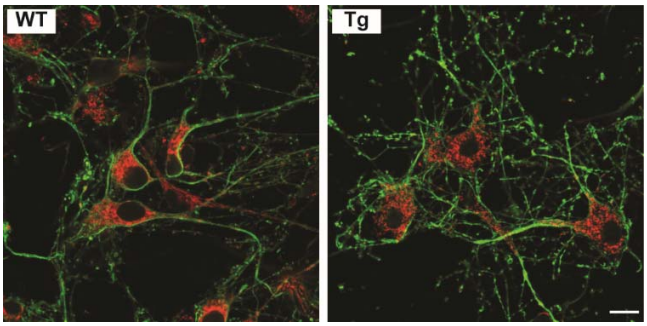

Figure S1. Visualization of hippocampal primary neuronal cultures. Primary neurons were cultured *in vitro* for 7 days and then fixed and stained to observe general morphology. Neurons were incubated with antibodies against βIII-tubulin (green) or Tom20 (red). Left panel, wild-type (WT) neurons. Right panel, transgenic (Tg) neurons. Scale bar, 200 µm.

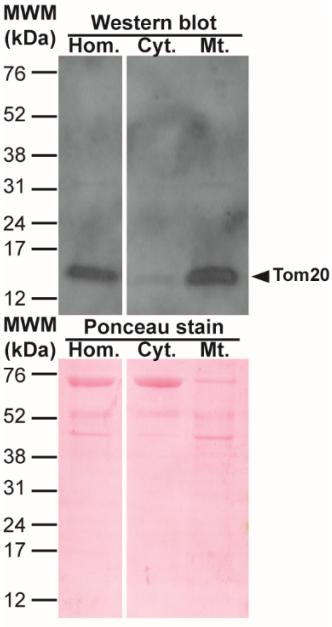

Figure S2. Quality control of the mitochondrial fraction used for LC-MS/MS global lipidomics. Upper panel, representative Western blotting of neuronal homogenates (Hom.), cytosolic (Cyt.) and mitochondrial (Mt) fractions immunoreacted with anti-Tom20 showing enrichment of mitochondria in Mt fraction used to assess lipidomics. Lower panel, protein content detected in each lane by Ponceau staining.

Table S1

Detectable free fatty acids and relative quantification in primary neurons of WT and Tg rats

	FFA (μM)			
	Palmitoleic	**Palmitic**	**Oleic**	**Stearic**
WT	0.99	5.70	2.40	4.50
	0.17	8.90	3.10	12.55
	0.30	6.20	18.00	9.10
Tg	0.99	6.65	7.55	9.55
	0.36	8.00	11.15	9.30
	0.59	4.30	1.40	4.60
t	0.50	0.42	0.19	0.31
α	0.63	0.69	0.85	0.76

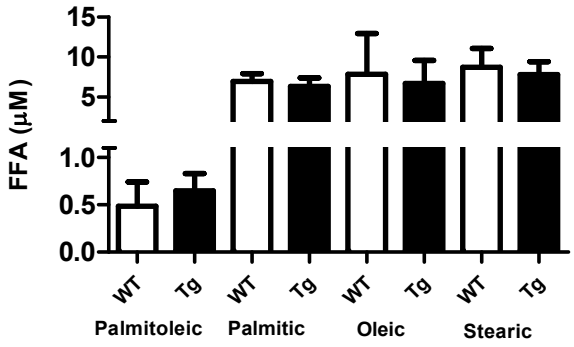

Three independent hippocampal primary neuronal cultures/genotype were performed using 10-12 embryos/culture. Free fatty acids (FFAs) row data from 3 biological samples (2 technical replicates) are provided in micromolar as extracted and do not represent the endogenous concentration. Inset, bars show mean ± SEM. A multiple t-test comparison was carried out in Prism between WT and Tg samples, but no significant ($p<0.05$) differences were observed for any of the detected FFAs.

Table S2. Complete list of lipid names and relative quantification in mitochondrial extracts of WT and Tg neurons

Lipid short name	Retention time (min)	Nominal mass	WT Average	Tg Average	P value WT vs Tg
plasmenyl-PE 36:4	13.7	722	17272843	9522255	0.001
CerP 42:4	13.7	722	17272843	9522255	0.001
PE 37:6	13.8	748	20311364	8825412	0.002
PC 20:0	15.5	624	17433948	28166667	0.005

DGDG 15:0	15.3	653	8904623	2098453	0.005
PC 34:1	13.9	818	49591234	30354157	0.007
PC 33:2	14.3	744	5410326	2372405	0.008
DG 34:1	15.3	612	12199583	3434804	0.009
PC 27:1	16	706	9165131	3124040	0.009
PI 38:4	8.3	885	11002317	2425867	0.010
DG 40:6	16	686	3415746	7078109	0.011
DG 38:4	15.3	662	8574788	3396817	0.012
CL 76:11	13.5	748	618420	249091	0.015
PE 36:2	14.2	744	16467800	5415078	0.015
PE 38:5	13.2	766	4311464	1382650	0.016
N-(15Z-tetracosenoyl)-sphing-4-enine	16	649	7726961	3056306	0.017
SM 40:1	15.3	788	3608982	856401	0.017
PC 40:6	13.7	834	6210569	2631169	0.020
PC 38:3	13.7	834	6210569	2631169	0.020
plasmenyl-PE 38:5	14.1	748	11115329	4972135	0.022
plasmenyl-PE 38:4	14.4	750	15223092	7415644	0.022
PE 37:5	14.4	750	15223092	7415644	0.022
plasmenyl-PE 38:6	13.4	746	8044789	2688952	0.023
PC 35:1	14.3	832	5422453	1324633	0.024
PC 36:1	14.7	846	15504496	7321780	0.027
PC 31:1	14.2	718	4301416	1764297	0.028
SM 36:1	13.8	732	13781411	7057502	0.028
PC 24:5	14	596	12313579	5660959	0.029
SM 34:1	11.5	704	9417851	2640561	0.032
SM 42:2	15.3	814	15735150	3656935	0.032
DG 38:6	15.5	658	3945400	6472196	0.033
PC 36:4	12.3	840	3581675	1699059	0.033
PC 36:8	14.3	774	15329783	3976324	0.034
plasmenyl-PE 34:1	14.5	700	21975474	8715185	0.036
PE 34:1	14.2	718	15109566	6876348	0.037
PC 36:2	14	844	15628949	6869951	0.041
PE 39:8	13.5	772	7644586	1865859	0.042
CerP 45:0	13.5	772	7644586	1865859	0.042
PC 31:4	13.9	734	102427232	56158573	0.043
PC 33:0	14.3	806	3811169	931700	0.043
PC 38:5	13.8	792	38201446	19646277	0.044
PC 35:5	14.7	788	39993681	19676793	0.046
PC 32:5	13.4	746	23122794	5452865	0.046
PE 36:1	14.9	746	16563712	7650983	0.047
PC 35:6	14	786	56923404	24813547	0.053
SM 38:1	14.7	760	3447997	1201630	0.053
PC 33:1	13.4	804	7430263	1546312	0.056
PC 40:5	14	836	6939986	3795618	0.056
plasmenyl-PE 40:6	14.3	774	9495351	3883077	0.057
PE 39:7	14.3	774	9495351	3883077	0.057
PC 18:0	14.8	538	13346498	21399766	0.058
DG 33:3	16	594	9798888	15814772	0.058
PC 22:0	16	594	9798888	15814772	0.058
PC 35:2	13.5	772	5933618	1048544	0.061

PC 33:5	13.9	760	165858048	100220475	0.061
NAE 20:0	6.1	414	815115	2320952	0.072
PC 31:0	13.2	778	5486193	1041844	0.072
PC 32:1	12.1	790	9629590	3021733	0.072
PE 35:3	14.6	726	16335639	4985161	0.073
MGDG 25:0	4.7	655	15675998	30988373	0.074
PC 40:7	12.4	816	2816095	750348	0.076
PC 38:2	14.7	814	5370441	1620407	0.076
MGDG 21:0	3.6	599	4899817	14314581	0.077
PC 32:4	14.3	748	11762381	2936383	0.080
MGDG 19:0	15.5	566	19086022	25541805	0.086
PI 38:3	10	887	3156354	364885	0.087
Sphingosine	3.6	358	11783302	27976669	0.091
plasmenyl-PE 40:4	14.9	778	8104350	3775774	0.092
PE 39:6	14.6	776	7012146	4054184	0.094
N-(octadecanoyl)-sphing-4-enine	14.8	567	12268813	5823270	0.097
PC 38:6	12.6	790	5781723	1866995	0.100
PC 31:5	12.6	732	18406535	6122249	0.102
DG 38:3	15.8	664	2880749	665473	0.104
plasmenyl-PE 36:1	15.2	728	7831717	2207787	0.107
TG 54:6	18	896	1627518	3268849	0.107
PC 36:0	14.5	812	7444758	2275498	0.111
PC 34:2	12.9	816	3434267	873320	0.112
N-(hexadecanoyl)-sphing-4-enine	14	539	5692769	3126846	0.112
CL 72:5	14.4	726	4585510	1992032	0.114
PC 30:0	11.7	764	6180809	2020744	0.116
PC 36:5	11.7	764	6180809	2020744	0.116
N,N-Dimethylsphingosine	4.7	386	46863544	88150719	0.122
PE 40:5	14.5	794	11809395	5359529	0.130
PC 37:6	14.8	776	8219032	4242501	0.139
PC 32:2	9.9	730	3491337	746643	0.144
PE 40:3	15.2	798	3856415	1040698	0.152
plasmenyl-PE 36:3	14.4	724	7547618	2321413	0.164
PC 36:3	13.8	842	3407141	908160	0.170
PE 40:4	14.7	796	5169800	3171569	0.177
PC 34:3	11.4	756	2475957	374768	0.183
CL 68:3	14.3	700	114744	53518	0.186
PC 21:0	14.8	624	19935115	7711044	0.192
plasmenyl-PE 38:3	14.9	752	5867230	1783285	0.193
PE 37:4	14.9	752	5867230	1783285	0.193
PE 38:4	14.2	768	31148033	19739020	0.211
plasmenyl-PE 40:5	14.8	776	7605888	3685472	0.215
PC 34:0	14.6	820	10151492	5080510	0.220
PE 40:6	14	792	7653199	4558131	0.230
PE 38:3	14.7	770	10905128	2855981	0.235
PC 32:0	13.8	778	6274307	4434874	0.240
PC 38:4	14	868	3786977	2705120	0.268
PI 6:0	1.6	445	3811843	3237211	0.498
MGDG 15:0	14.1	515	2540384	1418963	0.505
lysoPA 14:1	1.5	381	1086724	2134695	0.591

MG 22:6	1.5	409	11941124	11403416	0.619
MGDG 28:1	14.9	671	5076155	5173572	0.903
CL 74:3	14.2	742	35939	ND	NA

Three independent hippocampal primary neuronal cultures/genotype were performed using 10-12 embrios/culture and Mt isolated from each culture were processed independently. Unpaired two-tailed Student's t test was used for comparisons between genotypes.